




# Design of low cost, scalable, and high-performance $\text{TiS}_2$ thermoelectric materials via wet ball-milling process

Pandiyarasan Veluswamy<sup>1,2,\*</sup> , Saravanan Subramanian<sup>3,4,5</sup>, Muhmood ul Hassan<sup>6</sup>, Cafer T. Yavuz<sup>3</sup>, Ho Jin Ryu<sup>6</sup>, and Byung Jin Cho<sup>1,\*</sup>

<sup>1</sup> School of Electrical Engineering, Korea Advanced Institute of Science and Technology (KAIST), 291 Daehak-ro, Yuseong-gu, Daejeon 34141, Republic of Korea

<sup>2</sup> Flexible Thermoelectric Device Technology Center, Daejeon 34141, Republic of Korea

<sup>3</sup> Graduate School of EEWS, Korea Advanced Institute of Science and Technology (KAIST), 291 Daehak-ro, Yuseong-gu, Daejeon 34141, Republic of Korea

<sup>4</sup> Inorganic Materials and Catalysis Division, CSIR-Central Salt & Marine Chemicals Research Institute, Bhavnagar, Gujarat 364002, India

<sup>5</sup> Academy of Scientific and Innovative Research (AcSIR), Ghaziabad 201002, India

<sup>6</sup> Department of Nuclear and Quantum Engineering, KAIST, Daejeon 34141, Republic of Korea

Received: 18 April 2021

Accepted: 25 August 2021

Published online:

9 September 2021

© The Author(s), under exclusive licence to Springer Science+Business Media, LLC, part of Springer Nature 2021

## ABSTRACT

Thermoelectric (TE) materials could provide an efficient means for recovering waste heat energy if a low cost, scalable, and high figure-of-merit material could be fabricated. Here, we report, for the first time, a wet ball-milling method to achieve high-performance two-dimensional (2D) semi-metallic  $\text{TiS}_2$  nanoplatelets.  $\text{TiO}_2$  is milled, annealed, and sintered with sulfur under high pressure. The addition of a small amount of sulfur (S) powder during the annealing period prevents sulfur deficiency in the sintered compact, resulting in the formation of a near-stoichiometric  $\text{TiS}_2$  composition. The formation of 2D  $\text{TiS}_2$  nanoplatelets was confirmed by X-ray diffraction, field emission scanning electron microscopy with energy-dispersive spectroscopy, and X-ray photoelectron spectroscopy. The TE properties were measured in the temperature range of 25–100 °C. Further, we obtain that the prepared  $\text{TiS}_2$  has as high figure of merit as 0.35 at 100 °C. Novel wet ball mill processing strategies for the development of high-performance 2D materials such as  $\text{TiS}_2$  make it possible to incorporate these materials for scaled-up device fabrication.

Address correspondence to E-mail: pandiyarasan@yahoo.co.in; elebjcho81@kaist.ac.kr

## 1 Introduction

The last decade has seen significant progress in the field of nanoscale thermoelectric materials and their promising application in the energy field. The key factors contributing to the continuing interest in new thermoelectric materials are their potential to efficiently generate electrical power from waste heat without moving parts and serve as a long-lived power source at lower production cost and increased scalability, with no side effects or environmental harm, free from gas emissions. All these factors make them sustainable too.

The efficiency and performance of TE devices are described by the dimensionless figure of merit ( $ZT$ ) of the TE materials, defined as  $ZT = (S^2\sigma/\kappa) T$ , where  $S$  is the Seebeck coefficient,  $\sigma$  is the electrical conductivity,  $\kappa$  is the total thermal conductivity, and  $T$  is the absolute temperature [1–3]. Remarkable progress has been made toward developing high  $ZT$  TE materials, largely by tuning electron and phonon transport in the materials by lowering the thermal conductivity ( $\kappa$ ) and substantial power factor ( $S^2\sigma$ ) without affecting carrier mobility in the electron crystal region [4, 5]. For the past 50 years, thermoelectric applications with operating temperatures below 300 °C have typically employed bismuth telluride and lead telluride. They are the best-known TE materials in terms of performance with the optimum  $ZT$  values around 1. However, tellurides have limited availability and high cost, and, so, alternative materials with lower cost are being widely sought for large-scale applications [6, 7].

Transition metals have emerged as a new class of thermoelectric materials.  $\text{TiO}_2$ , in particular, has been sought for TE modules, mainly due to its low thermal conductivity. It is also readily available and non-toxic in nature. In addition, as-prepared  $\text{TiO}_2$  exhibits  $n$ -type conductivity, a consequence of its native defects [8]. However, it exhibits intermediate ionicity between fully ionic ( $\text{Ti}^{4+}$  and  $\text{O}^{2-}$ ) and covalent bond characteristics, and the asperous estimate indicates a charge of about + 2 on Ti and – 1 on O; the electron density of oxygen in  $\text{TiO}_2$  is lower than that of the aforementioned ionic crystals [9, 10]. Crucially, such defects are formed by ejecting oxygen from the lattice of  $\text{TiO}_2$  followed by the migration of dopant elements [11, 12].

As mentioned earlier, to understand the migration of defects in  $\text{TiO}_2$ , previous reports have suggested

several possible mechanisms: (1) that the surface defects of  $\text{TiO}_2$  nanoparticles can migrate more easily than bulk defects; (2) that an increase in interstitial defects occurs due to the formation of surface vacancies induced by reduction of the Ti–Ti interlayer distance; and (3) that diffusion defects occur easily along the  $c$  axis on the O site. The surface vacancies tend to lose oxygen and are relatively easier to generate and compare to Ti interstitials. The defect formation and migration energies can be achieved via heat treatment under a reducing atmosphere [13–15].

At the same time, two-dimensional (2D) transition metal dichalcogenide (TMDC) sulfide materials offer several advantages. They are environmental benign, have low toxicity, low cost, and mechanical flexibility, and they are abundant. Among them,  $\text{TiS}_2$  has demonstrated significant progress as a substitute TE material. Its power factor values are close to those of bismuth telluride in the  $n$ -type TE community [16–19]. For example, Imai et al. [20] revealed an exceptional thermopower value for  $\text{TiS}_2$ , with a single crystal Seebeck coefficient of about  $-250 \mu\text{V K}^{-1}$  at 300 K;  $n$ -type behavior and a relatively low resistivity of about  $1.7 \text{ m } \Omega \text{ cm}$  at 300 K. Despite this, the compound went largely unnoticed in the following years, until recently a few publications on this layered 2D structure reported that  $\text{TiS}_2$  has great potential as a TE material at low and medium temperatures.

Bourgès et al. [21] widely studied the formation of  $\text{TiS}_2$  via mechanical milling utilizing bulk  $\text{TiS}_2$ , and they obtained a low crystallite grain size according to the Debye–Callaway model. A low crystallite size leads to a structural level reduction in thermal conductivity. The reduction in the mean free path of phonons and an increase in grain boundary scattering led to a slight improvement in  $ZT$ , up to 0.3 at 700 K. Ohta et al. [22] optimized the synthesis parameter to form  $\text{TiS}_2$  via sulfurization of  $\text{TiO}_2$  with  $\text{CS}_2$  gas. The prepared  $\text{TiS}_2$ -sintered compacts with near-stoichiometric and titanium-rich compositions were measured along the directions perpendicular (in-plane) and parallel (out-plane) to the pressure applied, within the temperature range of 300–723 K. The highest  $ZT$  of 0.34 at 663 K was observed in the in-plane direction. Barbier et al. [23] described the intercalation of Ag cations in the van der Waals gap of stage 1- and stage 2-based  $\text{TiS}_2$  structures, which remarkably reduced the lattice thermal conductivity

through structural disorder. To tune the carrier concentration and to enhance the power factor in the specific temperature range, the intercalated silver provides additional carriers through charge transfer and ZT of 0.45 was achieved at 700 K.

Unfortunately, an overview of  $\text{TiS}_2$  composed of light elements found that it was unfavorable for phonon scattering, and a thermal conductivity of around  $4 \text{ Wm}^{-1} \text{ K}^{-1}$  was typically observed at room temperature in pristine single crystals or bulk materials [24]. This motivated the present work to develop a strategy of synthesis of an *n*-type  $\text{TiS}_2$  compound which offers an enormous reduction in thermal conductivity with enhanced ZT value, while maintaining high electrical performance.

To address all these advantages discussed above, the present study aimed to determine the efficiency of wet ball-milled  $\text{TiO}_2$  and/or S toward abatement in the liquid phase to form  $\text{TiS}_2$ . We examined the bonding of sulfur and the formation of  $\text{TiS}_2$  aggregates on the oxide surface. The mechanism of  $\text{TiS}_2$  formation could possibly involve the migration of O vacancies or Ti interstitials from the surface of the oxide, which then play a role in the generation of  $\text{TiS}_2$ . This approach is attractive, since the  $\text{TiO}_2$  precursor could potentially enable large yield, opening the possibility of large-scale production of TE devices.

## 2 Materials and methods

All the chemicals were purchased from Sigma-Aldrich with 99% purity. The initial precursor was commercial  $\text{TiO}_2$ -P25 and sulfur with tetrahydrofuran (THF) liquid phase was used as a preparatory material. Also, it is important to mention that the chemical stability of the material relies on the formation mechanism and it is affected by both the synthetic and post-synthetic processes.

Figure 1 shows a schematic representation of the  $\text{TiS}_2$  preparation. Briefly, calculated amounts of  $\text{TiO}_2$  and sulfur (15 g:5 g; 10 g:10 g; 5 g:15 g are named TS1; TS2; TS3) were placed into a ball mill under wet milling conditions using a high energy planetary ball mill (HEBM; Retsch Planetary PM100, Germany). The jar and milling media employed were made of Zirconia. 250 ml zirconia jars were filled with 400 g of zirconia balls (10 mm diameter) as milling media. The ratio between the weight of the balls and the powder

was 20:1, and a speed of 400 rotations per minute was used for a milling time of 24 h, with a regular interval of 3 min for every 1-h milling cycle, at room temperature.

The topotactic transformation of spherical  $\text{TiO}_2$  into 2D platelet  $\text{TiS}_2$  using the wet milling process with subsequent annealing is schematically shown in Fig. 1.

Among the predetermined ratios of  $\text{TiO}_2$  and sulfur combinations, a lower sulfur content causes less interaction and affects the complete formation of the  $\text{TiS}$  material. We expect that elemental sulfur first reduces  $\text{TiO}_2$  to metallic Titanium (Eq. 1). This is followed by the rapid sulfide formation of Ti into  $\text{TiS}$  (Eq. 2). The overall assumed reaction is, therefore, the reduction/oxidation combination, both facilitated by sulfur (Eq. 3).



An increase in the sulfur content also causes a detrimental effect, self-assembly induced by the S–S interaction, which restricts the formation of an orderly arranged  $\text{TiS}$  material. This clearly suggests the need for a delicate balance between  $\text{TiO}_2$  and sulfur to form the  $\text{TiS}$  material. This is the first observed case where deliberately ball milling  $\text{TiS}$  materials combines both physical and chemical routes into a single step [25]. In this process, sulfur helps to reduce  $\text{TiO}_2$  and generate the low-valent metallic titanium species which further interacts with the sulfur to form  $\text{TiS}$ .

After milling, the light-gray powder ( $\text{TiS}$ ) was finely ground and subsequently annealed at 300 °C for 3 h. The formed  $\text{TiS}$  was pyrolyzed with 0.2 mol equivalent of elemental sulfur to form  $\text{TiS}_2$ . The material was allowed to cool down to room temperature naturally. Then, to achieve an oriented compact with a highly sintered density, we performed inductive hot pressing at 200 °C for 10 min. The final dimensions of each pellet were around 12 mm in diameter and 5 mm in thickness. A dense formation of  $\text{TiS}_2$  nanoplatelets was observed and further characterized.

The phase constitution and structural properties of the samples were determined by X-ray diffraction

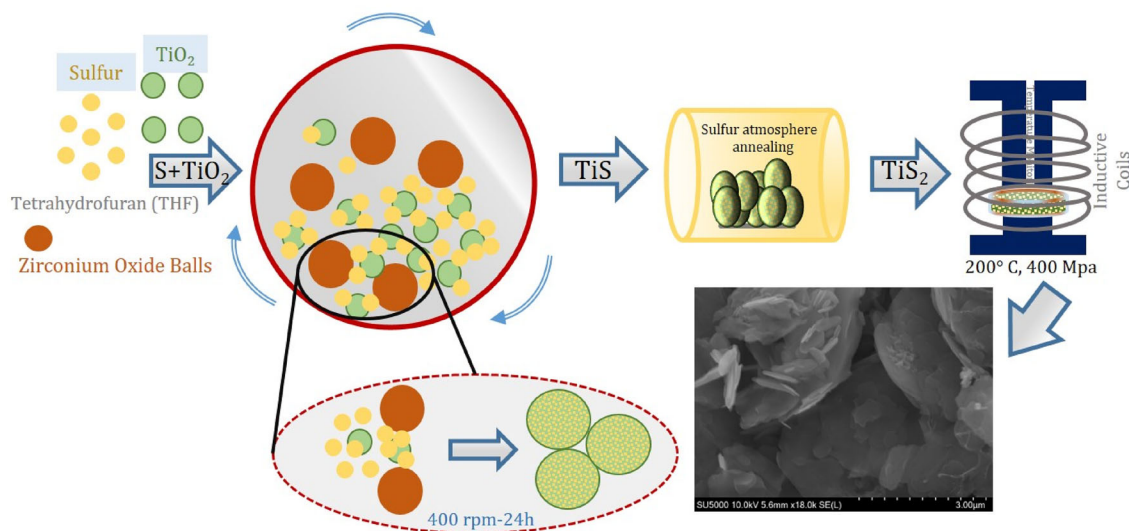


**Fig. 1** Materialization mechanism of  $\text{TiO}_2$  to  $\text{TiS}_2$

analysis. The microstructure and elemental analysis were examined using a field emission secondary electron microscope equipped with an energy-dispersive spectroscopy (EDS). The bonding state of titanium to sulfur in the prepared samples was investigated by X-ray photoelectron spectroscopy. The carrier concentration was determined by Hall Effect measurement with a van der Pauw electrode configuration at room temperature in a constant magnetic field (1 T) and a constant electrical current of 50 mA. The electrical conductivity and Seebeck coefficient were measured using disc-shaped samples in an argon atmosphere from 25 to 100 °C. The thermal conductivity can be calculated using the equation:  $\kappa = C_p \times d \times \lambda$ , where  $C_p$ ,  $d$ , and  $\lambda$  are specific heat, density, and thermal diffusivity, respectively. The thermal diffusivity was measured by a laser flash method in an argon atmosphere. The specific heat capacity was measured by differential scanning calorimeter. The density measurement was carried out by a He Gas Pycnometer.

### 3 Results and discussion

The XRD patterns of the as-purchased P25- $\text{TiO}_2$  attributed to an anatase–rutile phase with the surface OH density [26]. Sulfur will react with the functional group and absorb water molecules, which results in the formation of  $\text{H}_2\text{S}$  gas and favors the formation of Ti–S groups [22]. During wet ball milling, the mechanical activation energy will break the partial

surface layer of Ti–O bonds and a low oxygen atmosphere will lead to oxygen vacancies. Since oxygen does not favor, increasing the milling time has a significant effect on the phase transformation, while the milling speed and the powder to ball ratio are the critical factors [15].

In Fig. 2i, the XRD diffraction pattern of TS1 prepared by wet ball milling shows the presence of sharp diffraction peaks which match the standard diffraction pattern of TiS (JCPDS No. 74-0139), without any detectable peaks of impurities. The diffraction peaks obtained at 20.15°, 30.94°, 38.61°, 41.89°, 51.81°, 54.70°, and 57.86° correspond to the (006), (012), (107), (018), (0015), (113), and (116) planes of the TiS with a space group of R-3 m (166). As in the case of TS2 & TS3, it indicates  $\text{Ti}_2(\text{SO}_4)_3$  which matches JCPDS No. 83-6405 [27, 28].

The chemical binding energies of the as-synthesized TiS and  $\text{Ti}_2(\text{SO}_4)_3$  were further evaluated by XPS analysis. As shown in Fig. 2ii, there were two strong Ti 2p peaks at 464.4 and 458.1 for TS1, 464.2 and 458.4 for TS2, and 464.2 and 458.5 for TS3, respectively, with a spin–orbit doublet splitting of 6.3, 5.8, and 5.7 eV matching closely the characteristics of the Ti peaks in TS1 and  $\text{Ti}^{3+}$  in TS2 and TS3. The S 2p spectra presented in (b), (c), and (d) are of TS1, TS2, and TS3, respectively. For TS1, the two peaks are assigned to the S 2p<sub>3/2</sub> and 2p<sub>1/2</sub> and  $\text{S}^{2-}$  and the fitted peak intensity ratio is 2:1, which refers S atoms that react with O sites near defects of the surface leading to TiS composed [29]. S 2p adsorption

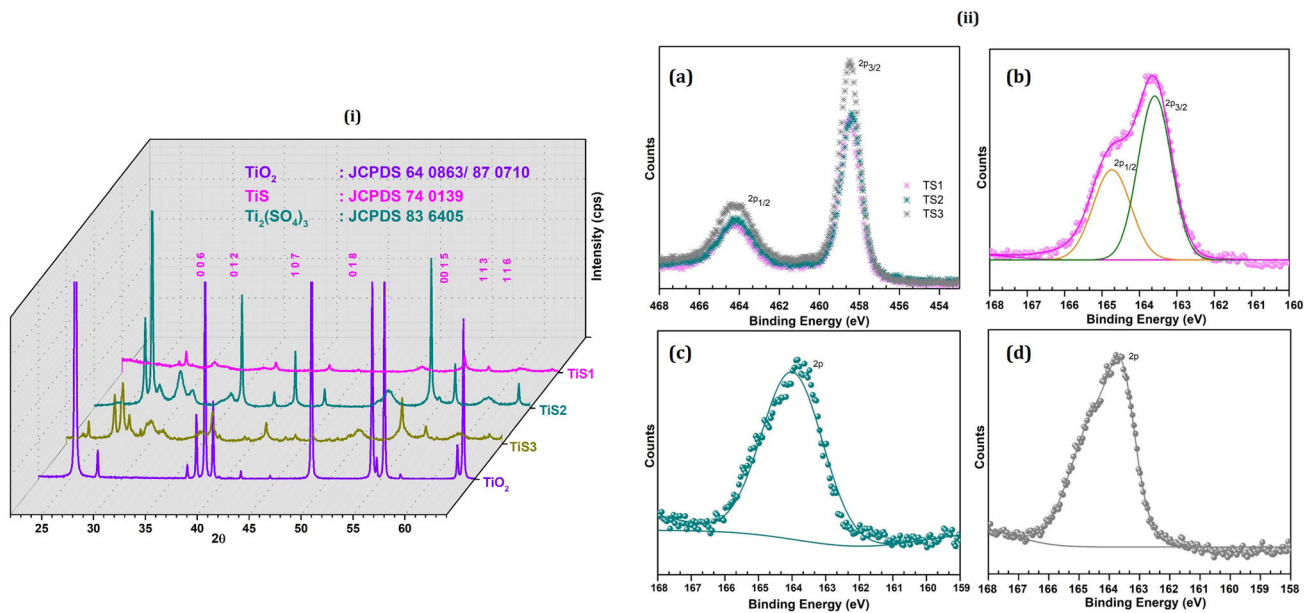


**Fig. 2** i XRD profile of as-purchased  $\text{TiO}_2$ , wet ball-milled  $\text{Ti}_2(\text{SO}_4)_3$  and  $\text{TiS}_2$ ; ii XPS core level spectra of Ti 2p (a) and S 2p (b–d)

in TS2 and TS3 leads to additional sulfur dosing, leading to saturation and S reaction with O bridging on the oxide surface. These contributions may account for the slight formation of  $\text{Ti}_2(\text{SO}_x)_{x-1}$  [30, 31].

The micrographs of the as-received  $\text{TiO}_2$  at low / high magnification and the superimposed mapping image in Fig. 3a–c show a spherical shape with an average diameter of 500 nm. A typical EDS mapping shows homogeneous distribution of Ti, O, and C (which appears due to the sample holder). The as-prepared wet-milled TS1 (TiS) is shown in Fig. 3d and e. A strong difference in contrast was observed in the recorded SEM images, and the platelets appear with a light contrast, suggesting the presence of heavy elements such as Ti. The dark contrast between the platelets' surface/edge indicates the presence of lighter elements such as S.

The differences in chemical composition mapping are evident between these regions and the platelets are shown in Fig. 3f. The TiS crystallites are about 10  $\mu\text{m}$  long and 1  $\mu\text{m}$  thick with a platelet shape, and it is apparent that the Ti region of particles is extremely dark compared with the S region. This is because they are highly oriented. From the TS2 and TS3 shown in Fig. 3g–l, it was found that an excessive amount of sulfur in the solution can probably delay the formation of orderly arranged TiS materials due to the detrimental effect of the S–S interaction [32].

The progressive phase formation of powder samples after the wet milling without (TS1a)/with (TS1sa) sulfur environmental annealing is shown in Fig. 4a. It was seen from the XRD profile that there might be two phases found, with the broad and sharp peaks corresponding to the JCPDS cards: 81-0687 and 80-4223 [27, 28]. The TS1sa absence of peak reveals that the effective role of S ions was facilitated by the migration of O vacancies or  $\text{Ti}^{3+}$  interstitials from the bulk to the surface of the oxide [33].

The morphology images are presented in Fig. 4b and c of the TS1a and TS1sa samples. In the TS1a sample, there is a distinct transformation from the irregular/angular shape of the starting TiS2 into small aggregates with well-organized shapes. The crystal orientation with anisotropic grain growth is mainly governed by the TiS2 structure which consists of chains or polyhedral layers. Close-packed atomic planes have low surface energy and are more thermodynamically stable [34]. Such planes also tend to be atomically smooth, making growth perpendicular to the plane difficult to nucleate. In addition, the sulfur annealing used in the solid–liquid–vapor reaction, as in the TS1a synthesis, favors the growth of these large plate-like crystallites. Examination of the fractured cross section by SEM revealed a dense structure, which is consistent with the results of EDS mapping (Fig. 4d).

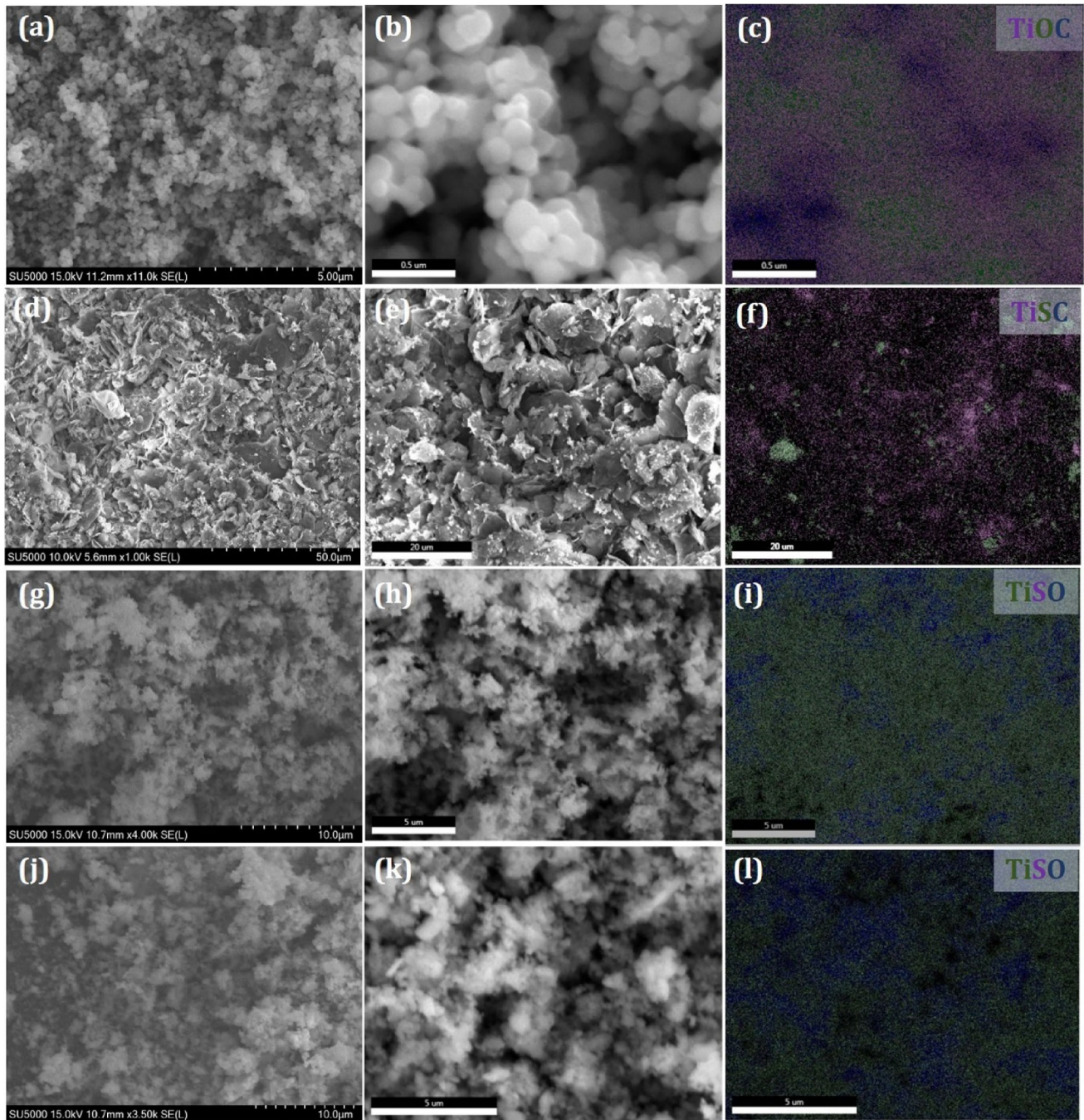
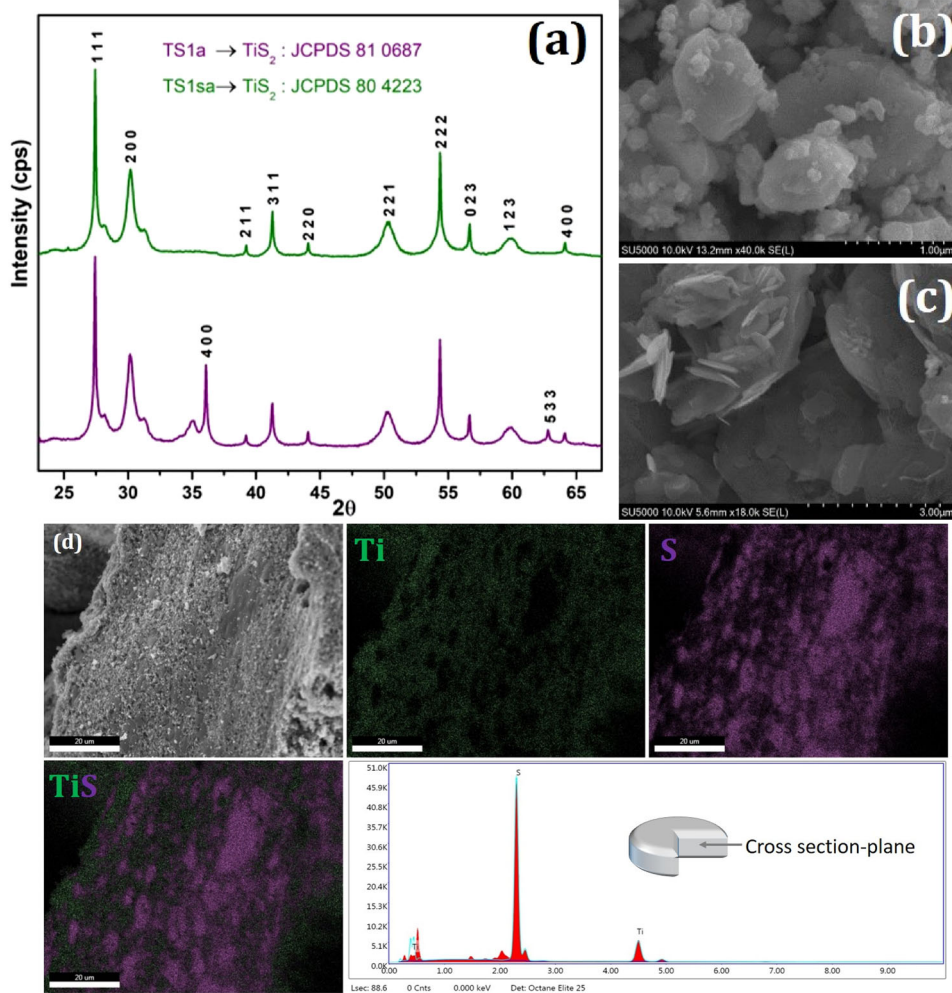


**Fig. 3** SEM images and corresponding EDS mapping of  $\text{TiO}_2$  (a–c), TS1 (d–f), TS2 (g–i), and TS3 (j–l)

All the samples showed highly degenerated semiconductor behavior in the extrinsic region and *n*-type behavior. The electron carrier concentration increased with annealing temperature and the pelletization process, as shown in Fig. 5a. The as-received  $\text{TiO}_2$  acts as an ineffective acceptor and thus the *n*-type conduction is formed [35]. TS1 (as-prepared-TiS), TS1a (annealed TiS), and TS1sa (sulfur annealed TiS)

are pellets prepared at room temperature. Similarly, HTS1, HTS1a, and HTS1sa are pellets prepared at 200 °C for 10 min under the uniaxial pressure of 400 MPa. The density of sulfur annealed/sintered is consistently lower than that of  $\text{TiO}_2$ . Most of the sulfur atoms, therefore, are expected to take part in the formation of both the surface and grain boundary layers. If all of the sulfur atoms dissolved in the

**Fig. 4** Various annealing conditions with/without sulfur annealed (TS1a/ TS1sa)  $\text{TiS}_2$  **a** XRD profile, **b**, **c** SEM images, and **d** cross-sectional SEM image with EDS mapping



matrix were removed, the electron concentration would be  $3.961 \times 10^{-19} \text{ m}^{-3}$ , which agrees well with the actual increased amount.

Based on the results of the sulfur annealed/sintered, we believe that the grain boundary density decreases and the electron carrier concentration increases. Indeed, the electron concentration increased from  $1.91 \times 10^{-17}$  to  $3.96 \times 10^{-19} \text{ m}^{-3}$  after sulfur annealing for 3 h and reached up to  $7.64 \times 10^{19} \text{ m}^{-3}$  with the subsequent hot sintering. This rate of increase can also be explained quantitatively by an increase in sulfur atoms dissolved in the matrix during sintering.

The temperature dependence of the electrical transport properties in the  $\text{TiS}_2$  sample is shown in Fig. 5b–d. The Seebeck coefficient as a function of temperature is displayed in Fig. 5b. The negative values of Seebeck coefficient indicate that all the samples are *n* type and the major carriers are

electrons. On the other hand, it shows the typical up-down behavior commonly found in 2D materials, which is mainly due to excitation of the minority carriers [36]. This figure suggests that all the samples show a nearly similar temperature-dependent behavior, which is in-line with those reported earlier for similar  $\text{TiS}_2$ -based material [37].

The Seebeck coefficient shows an increasing trend with increasing temperature due to intrinsic excitation of the charge carriers, which typically coincides with the performance of their bulk counterpart. The decrease in the Seebeck coefficient is attributed to thermal excitation of the charge carriers across the band gap.

In contrast, the Seebeck coefficient value was  $3.35 \times 10^{-05}$  to  $6.78 \times 10^{-05} \text{ V K}^{-1}$  for the temperature range of 25–100 °C because the sulfur was annealed with subsequent hot pressing at 200 °C. The electrical conductivity of the samples with respect to

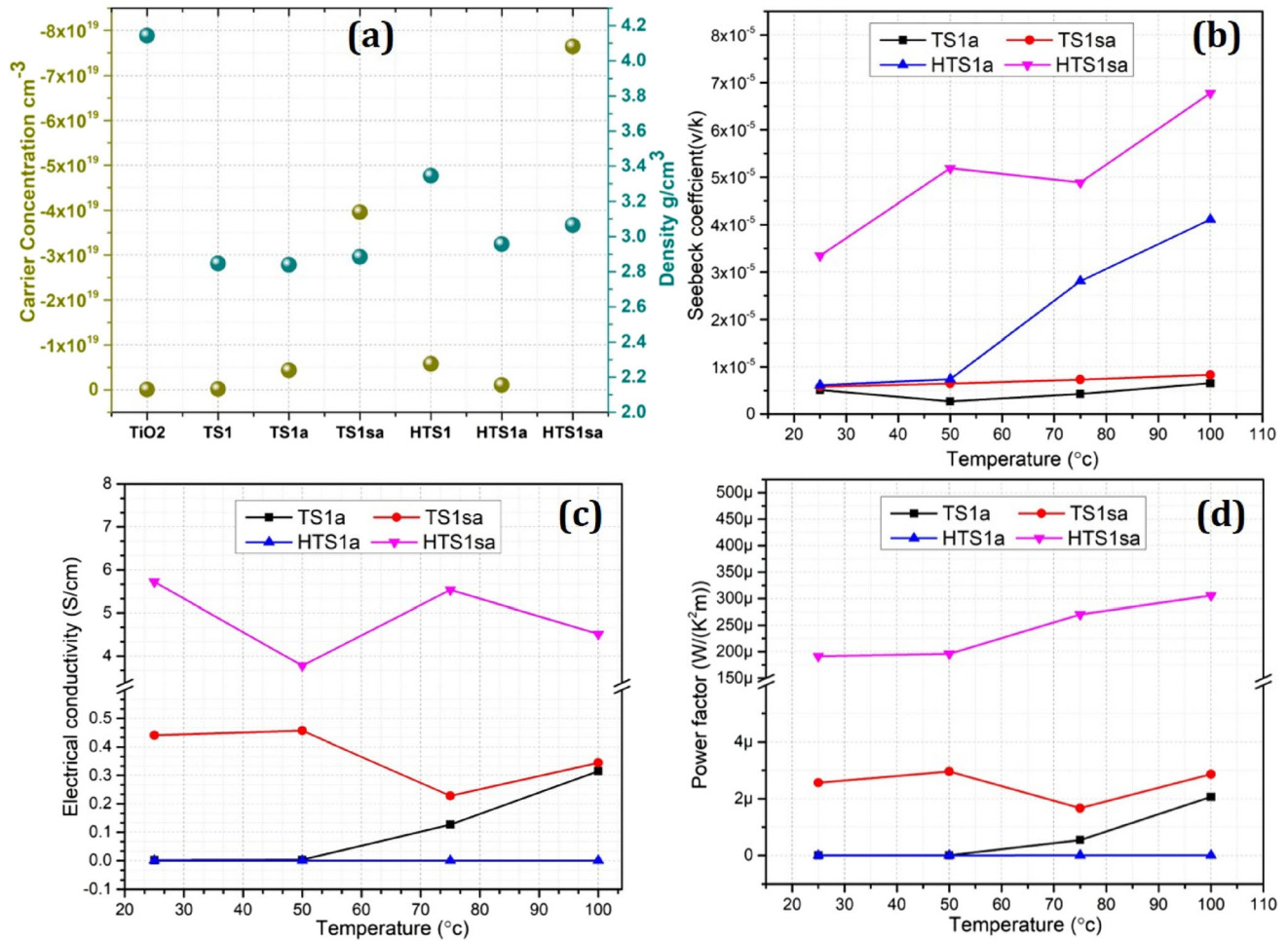


**Fig. 5** Transport properties of TiS<sub>2</sub> with (H)/without temperature hot press: **a** carrier concentration and density, **b** Seebeck coefficient, **c** electrical conductivity, and **d** power factor

the measured temperature is shown in Fig. 5c. All the samples showed highly degenerated semiconductor behavior in the extrinsic region. The stoichiometry ratio of Ti and S significantly influences the electrical transport properties of TiS<sub>2</sub>.

As a whole, the present results show some similarities to those reported for Ag<sub>x</sub>TiS<sub>2</sub> [38], where the charge-transfer mechanism was used to account for the observed phenomenon. The electrical conductivity value of HTS1sa is almost constant but with a small hump at 70 °C. This implies that the amount of S decreases slightly at 50 °C and remains almost constant up to 100 °C. It is reasonable to assume here that the valence electrons of the S atoms transfer to the Ti band of the host after intercalation, leading to an increase in electron concentration and enhancement of TiS<sub>2</sub> [39].

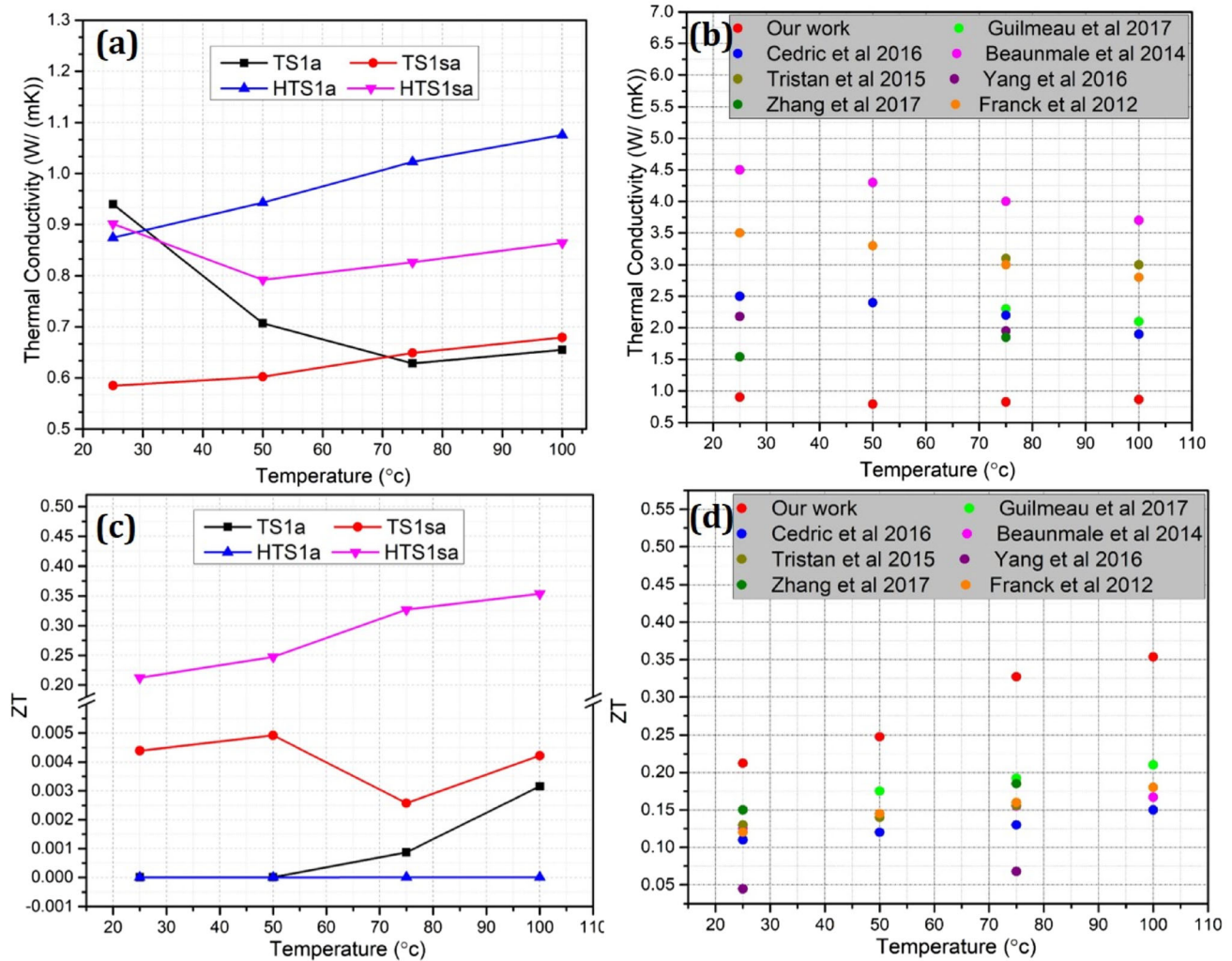
The thermoelectric power factor ( $S^2 \cdot \sigma$ ) of TiS<sub>2</sub> can be estimated from the  $S$  and  $\sigma$  values, as shown in

Fig. 5d. The sulfur annealed with hot pressing at 200 °C shows a better power factor of 300 μW K<sup>-2</sup>m at room temperature pressing. The total thermal conductivity  $\kappa$  total shown in Fig. 6a was estimated in the temperature range of 25–100 °C using the formula:  $\kappa$  total =  $C_p \times d \times \lambda$ , where  $C_p$ ,  $d$ , and  $\lambda$  are specific heat, density, and thermal diffusivity, respectively.

It can be seen that the annealing and sulfur annealing cause a large decrease in total thermal conductivity over the whole temperature range. The lattice thermal conductivity significantly increased when the sample underwent hot pressing. This increase in lattice thermal conductivity could be due to phonon scattering from the intercalated S atoms in the van der Waals gaps [40, 41].

In Fig. 6b, a comparison of the thermal conductivity performance is shown. All the values are measured as dependent on temperature. As can be seen





**Fig. 6**  $\text{TiS}_2$  with (H)/without temperature hot press. **a** Thermal conductivity of as-prepared and **b** comparative report so far in the thermal conductivity, **c** ZT efficiency of as-prepared and **d** benchmarking result with comparative report so far in ZT efficiency

in the results the wet ball milling shows the lowest values of thermal conductivity. This performance is attributed to an increase in grain boundary scattering due to the decrease in grain size and point defect scattering due to the S atoms.

Figure 6c shows the temperature dependence of the figure-of-merit ZT for  $\text{TiS}_2$ . The ZT values of all the samples tended to increase with increasing temperature. However, the ZT value for the annealed TS1sa is slightly lower than that of hot-pressed annealed HTS1sa because of the large decrease in their thermopower, although their resistivity and thermal conductivity decreased considerably [42, 43].

However, ZT of hot-pressed HTS1sa was substantially improved over the whole temperature range under consideration. Evidently, this improvement in

the thermoelectric properties of  $\text{TiS}_2$  can be attributed to the increase in Seebeck coefficient, resulting from increased carrier concentration due to charge transfer and decrease in lattice thermal conductivity presumably caused by the vibration of S atoms in the van der Waals gaps of the  $\text{TiS}_2$ . A benchmark comparison of ZT values with our results as a function of temperature is shown in Fig. 6d.

## 4 Conclusion

In the past decade, various strategies have been explored to enhance power generation performance by reducing lattice thermal conductivity in TE materials, which consequently increases their ZT

performance. The thermoelectric properties of  $\text{TiS}_2$  prepared by wet ball milling with a subsequent sulfur annealing and hot press sintering showed a highest ZT of 0.35 at 100 °C. In addition, the transport properties of carrier concentration were also investigated at room temperature. A significant enhancement in the ZT value was observed because of the higher Seebeck coefficient, high electrical conductivity, and relatively low thermal conductivity of  $0.1 \text{ W K}^{-1} \text{ m}^{-1}$ .

## Acknowledgements

This work was supported by a grant from the National Research Foundation of Korea funded by the Korean government (MSIP) (NRF-2015R1A5A1036133).

## References

- P. Veluswamy, S. Sathiyamoorthy, F. Khan, A. Ghosh, M. Abhijit, Y. Hayakawa, H. Ikeda, Incorporation of ZnO and their composite nanostructured material into a cotton fabric platform for wearable device applications. *Carbohydr. Polym.* **157**, 1801–1808 (2017)
- S. Sathiyamoorthy, G. Girijakumari, P. Kannan, K. Venugopal, S.T. Shanmugam, P. Veluswamy, K.D. Wael, H. Ikeda, Tailoring the functional properties of polyurethane foam with dispersions of carbon nanofiber for power generator applications. *Appl. Surf. Sci.* **449**, 507–513 (2018)
- I. Hiroya, K. Faizan, V. Pandiyarasan, S. Shota, N. Mani, S. Masaru, M. Kenji, H. Yasuhiro, Thermoelectric characteristics of nanocrystalline ZnO grown on fabrics for wearable power generator. *J. Phys. Conf. Ser.* **1052**(1), 012017 (2018)
- F. Trier, D.V. Christensen, N. Pryds, Electron mobility in oxide heterostructures. *J. Phys. D Appl. Phys.* **51**(29), 293002 (2018)
- X. Zhang, L.-D. Zhao, Thermoelectric materials: energy conversion between heat and electricity. *J. Mater.* **1**(2), 92–105 (2015)
- A.D. LaLonde, Y. Pei, H. Wang, G. Jeffrey Snyder, Lead telluride alloy thermoelectrics. *Mater. Today* **14**(11), 526–532 (2011)
- J.H. Goldsmid, Bismuth telluride and its alloys as materials for thermoelectric generation. *Materials* **7**(4), 2577–2592 (2014)
- M.A. Henderson, A surface perspective on self-diffusion in rutile  $\text{TiO}_2$ . *Surf. Sci.* **419**(2), 174–187 (1999)
- S. Wendt, P.T. Sprunger, E. Lira, G.K.H. Madsen, Z. Li, J. Hansen, J. Matthiesen, A. Blekinge-Rasmussen, E. Lægsgaard, B. Hammer, F. Besenbacher, The role of interstitial sites in the Ti3d defect state in the band gap of titania. *Science* **320**(5884), 1755 (2008)
- R. Amade, P. Heitjans, S. Indris, M. Finger, A. Haeger, D. Hesse, Defect formation during high-energy ball milling in  $\text{TiO}_2$  and its relation to the photocatalytic activity. *J. Photochem. Photobiol. A* **207**(2), 231–235 (2009)
- S. Bai, N. Zhang, C. Gao, Y. Xiong, Defect engineering in photocatalytic materials. *Nano Energy* **53**, 296–336 (2018)
- J.-D. Peng, P.-C. Shih, H.-H. Lin, C.-M. Tseng, R. Vittal, V. Suryanarayanan, K.-C. Ho,  $\text{TiO}_2$  nanosheets with highly exposed (001)-facets for enhanced photovoltaic performance of dye-sensitized solar cells. *Nano Energy* **10**, 212–221 (2014)
- G. Fazio, L. Ferrighi, C. Di Valentin, Photoexcited carriers recombination and trapping in spherical vs faceted  $\text{TiO}_2$  nanoparticles. *Nano Energy* **27**, 673–689 (2016)
- Y. Zhang, J. Liu, Y. Zhang, Y. Bi, Relationship between interatomic electron transfer and photocatalytic activity of  $\text{TiO}_2$ . *Nano Energy* **51**, 504–512 (2018)
- M.K. Nowotny, L.R. Sheppard, T. Bak, J. Nowotny, Defect chemistry of titanium dioxide. Application of defect engineering in processing of  $\text{TiO}_2$ -based photocatalysts. *J. Phys. Chem. C* **112**(14), 5275–5300 (2008)
- R. Zhang, C. Wan, Y. Wang, K. Koumoto, Titanium sulphene: two-dimensional confinement of electrons and phonons giving rise to improved thermoelectric performance. *Phys. Chem. Chem. Phys.* **14**(45), 15641–15644 (2012)
- A. Amara, Y. Frongillo, M.J. Aubin, S. Jandl, J.M. Lopez-Castillo, J.P. Jay-Gerin, Thermoelectric power of  $\text{TiS}_2$ . *Phys. Rev. B* **36**(12), 6415–6419 (1987)
- C. Wan, Y. Wang, N. Wang, K. Koumoto, Low-thermal-conductivity  $(\text{MS})_{1+x}(\text{TiS}_2)_2$  ( $M = \text{Pb}, \text{Bi}, \text{Sn}$ ) misfit layer compounds for bulk thermoelectric materials. *Materials* **3**(4), 2606–2617 (2010)
- K. Sánchez, P. Palacios, P. Wahnón, Electronic structure of bulk- and Na-intercalated  $\text{TiS}_2$  determined from a GGA+U study with the Hubbard terms obtained ab initio. *Phys. Rev. B* **78**(23), 235121 (2008)
- H. Imai, Y. Shimakawa, Y. Kubo, Large thermoelectric power factor in  $\text{TiS}_2$  crystal with nearly stoichiometric composition. *Phys. Rev. B* **64**(24), 241104 (2001)
- C. Bourgès, T. Barbier, G. Guélou, P. Vaquero, A.V. Powell, O.I. Lebedev, N. Barrier, Y. Kinemuchi, E. Guilmeau, Thermoelectric properties of  $\text{TiS}_2$  mechanically alloyed compounds. *J. Eur. Ceram. Soc.* **36**(5), 1183–1189 (2016)

22. M. Ohta, S. Satoh, T. Kuzuya, S. Hirai, M. Kunii, A. Yamamoto, Thermoelectric properties of  $Ti_{1+x}S_2$  prepared by  $CS_2$  sulfurization. *Acta Mater.* **60**(20), 7232–7240 (2012)
23. T. Barbier, O.I. Lebedev, V. Roddatis, Y. Bréard, A. Maignan, E. Guilmeau, Silver intercalation in SPS dense  $TiS_2$ : staging and thermoelectric properties. *Dalton Trans.* **44**(17), 7887–7895 (2015)
24. E. Guilmeau, A. Maignan, C. Wan, K. Koumoto, On the effects of substitution, intercalation, non-stoichiometry and block layer concept in  $TiS_2$  based thermoelectrics. *Phys. Chem. Chem. Phys.* **17**(38), 24541–24555 (2015)
25. J. Xu, J. Shui, J. Wang, M. Wang, H.-K. Liu, S.X. Dou, I.-Y. Jeon, J.-M. Seo, J.-B. Baek, L. Dai, Sulfur–graphene nanostructured cathodes via ball-milling for high-performance lithium–sulfur batteries. *ACS Nano* **8**(10), 10920–10930 (2014)
26. A. Holm, M. Hamandi, F. Simonet, B. Jouguet, F. Dappozze, C. Guillard, Impact of rutile and anatase phase on the photocatalytic decomposition of lactic acid. *Appl. Catal. B* **253**, 96–104 (2019)
27. C.S. Cucinotta, K. Dolui, H. Pettersson, Q.M. Ramasse, E. Long, S.E. O’Brian, V. Nicolosi, S. Sanvito, Electronic properties and chemical reactivity of  $TiS_2$  nanoflakes. *J. Phys. Chem. C* **119**(27), 15707–15715 (2015)
28. S.B. Basuvalingam, Y. Zhang, M.A. Bloodgood, R.H. Godiksen, A.G. Curto, J.P. Hofmann, M.A. Verheijen, W.M.M. Kessels, A.A. Bol, Low-temperature phase-controlled synthesis of titanium di- and tri-sulfide by atomic layer deposition. *Chem. Mater.* **31**(22), 9354–9362 (2019)
29. J.A. Rodriguez, J. Hrbek, Z. Chang, J. Dvorak, T. Jirsak, A. Maiti, Importance of O vacancies in the behavior of oxide surfaces: adsorption of sulfur on  $TiO_2$  (110). *Phys. Rev. B* **65**(23), 235414 (2002)
30. C.G. Hawkins, L. Whittaker-Brooks, Controlling sulfur vacancies in  $TiS_{2-x}$  cathode insertion hosts via the conversion of  $TiS_3$  nanobelts for energy-storage applications. *ACS Appl. Nano Mater.* **1**(2), 851–859 (2018)
31. H. Jing, Q. Cheng, J.M. Weller, X.S. Chu, Q.H. Wang, C.K. Chan, Synthesis of  $TiO_2$  nanosheet photocatalysts from exfoliation of  $TiS_2$  and hydrothermal treatment. *J. Mater. Res.* **33**, 1–9 (2018)
32. M. Birkholz, R. Rudert, Interatomic distances in pyrite-structure disulfides—a case for ellipsoidal modeling of sulfur ions. *Physica Status Solidi (b)* **245**(9), 1858–1864 (2008)
33. S.G. Kumar, K.S.R.K. Rao, Polymorphic phase transition among the titania crystal structures using a solution-based approach: from precursor chemistry to nucleation process. *Nanoscale* **6**(20), 11574–11632 (2014)
34. J. Ma, H. Jin, X. Liu, M.E. Fleet, J. Li, X. Cao, S. Feng, Selective synthesis and formation mechanism of  $TiS_2$  dendritic crystals. *Cryst. Growth Des.* **8**(12), 4460–4464 (2008)
35. E.M. Logothetis, W.J. Kaiser, C.A. Kukkonen, S.P. Faile, R. Colella, J. Gambold, Hall coefficient and reflectivity evidence that  $TiS_2$  is a semiconductor. *J. Phys. C Solid State Phys.* **12**(13), L521 (1979)
36. Y. Ye, Y. Wang, Y. Shen, Y. Wang, L. Pan, R. Tu, C. Lu, R. Huang, K. Koumoto, Enhanced thermoelectric performance of  $xMoS_2$ – $TiS_2$  nanocomposites. *J. Alloys Compd.* **666**, 346–351 (2016)
37. J.-H. Pöhls, A. Faghaninia, G. Petretto, U. Aydemir, F. Ricci, G. Li, M. Wood, S. Ohno, G. Hautier, G.J. Snyder, G.-M. Rignanese, A. Jain, M.A. White, Metal phosphides as potential thermoelectric materials. *J. Mater. Chem. C* **5**(47), 12441–12456 (2017)
38. M. Beaumale, T. Barbier, Y. Bréard, G. Guelou, A.V. Powell, P. Vaqueiro, E. Guilmeau, Electron doping and phonon scattering in  $Ti_{1+x}S_2$  thermoelectric compounds. *Acta Mater.* **78**, 86–92 (2014)
39. F. Mendizabal, R. Contreras, A. Aizman, A model for the charge capacity of  $1T$ – $TiS_2$  intercalated with Li. *Int. J. Quantum Chem.* **56**(6), 819–823 (1995)
40. H. Euchner, S. Pailhès, V.M. Giordano, M. de Boissieu, Understanding lattice thermal conductivity in thermoelectric clathrates: a density functional theory study on binary Si-based type-I clathrates. *Phys. Rev. B* **97**(1), 014304 (2018)
41. B. Fu, G. Tang, Y. Li, Electron–phonon scattering effect on the lattice thermal conductivity of silicon nanostructures. *Phys. Chem. Chem. Phys.* **19**(42), 28517–28526 (2017)
42. P. Zou, G. Xu, S. Wang, P. Chen, F. Huang, Effect of high pressure sintering and annealing on microstructure and thermoelectric properties of nanocrystalline  $Bi_2Te_{2.7}Se_{0.3}$  doped with Gd. *Prog. Nat. Sci. Mater. Int.* **24**(3), 210–217 (2014)
43. X. Yan, E. Bauer, P. Rogl, S. Paschen, Influence of hot pressing temperature on thermoelectric properties of type-I clathrates. *Physica Status Solidi (a)* **211**(6), 1282–1287 (2014)

**Publisher’s Note** Springer Nature remains neutral with regard to jurisdictional claims in published maps and institutional affiliations.